Chapter 14

Wavefunction Analysis of STM Image: Surface Reconstruction of Organic Charge Transfer Salts

Hirokazu Sakamoto, Eiichi Mori, Hideyuki Arimoto, Keiichiro Namai, Hiroyuki Tahara, Toshio Naito, Taka-aki Hiramatsu, Hideki Yamochi and Kenji Mizoguchi

Additional information is available at the end of the chapter

http://dx.doi.org/10.5772/63406

Abstract

In this chapter, the wavefunction analysis is demonstrated, applied to the organic charge transfer salts composed of electron donor and electron acceptor molecules. Scanning tunneling microscopy (STM) images of the surface donor layers in the three charge transfer salts, α-(BEDT-TTF)$_2$I$_3$, β-(BEDT-TTF)$_2$I$_3$, and (EDO-TTF)$_2$PF$_6$, are analyzed with the atomic π electron orbitals of sulfur, oxygen, and carbon atoms. We have deduced three different kinds of surface molecular reconstructions as follows: (1) charge redistribution in α-(BEDT-TTF)$_2$I$_3$, (2) translational reconstruction up to 0.1 nm in β-(BEDT-TTF)$_2$I$_3$, and (3) rotational reconstruction transforming the 1D axis from the *a* axis to the *b* axis in (EDO-TTF)$_2$PF$_6$. Finally, it is concluded that the surface reconstruction is ascribed to the additional gain of the cohesive energy of the π electron system, provoked by the reduced steric hindrance with the anions of the missing outside double layer. The investigations of the surface states provide not only interesting behaviors of the surface cation layer, but also important insights into the electronic states of a lot of similar charge transfer crystals, as demonstrated in α-(BEDT-TTF)$_2$I$_3$.

Keywords: STM, surface reconstruction, charge reorientation, translational reconstruction, rotational reconstruction, organic charge transfer salt, wavefunction analysis, topography

1. Introduction

It is well known that scanning tunneling microscopy (STM) is a powerful tool to disclose the atomic images, and is applicable to the conducting materials, such as metals and semiconductors. However, since STM images are constructed with the electron tunneling probability between the wavefunctions of an STM probe tip and those of a sample surface, it is required for us to analyze the wavefunctions of the atoms and the molecules in the surface layer to extract structural information. In this chapter, some examples of the wavefunction analysis [1] are demonstrated in the organic charge transfer salts composed of electron donor and electron acceptor molecules, in which the van der Waals interaction and the π electron transfer integrals between like molecules, and the Coulomb attractive interaction between unlike molecules govern the formation of the crystals. Since the van der Waals interaction between the like molecules is relatively weak, the analysis of atomic π orbitals of sulfur, oxygen, and carbon atoms of the donor molecules would be a good approximation for the wavefunction analysis of STM images.

Organic charge transfer salts have been intensively investigated for a long period more than 40 years (for example, see [2]). The electronic states are mainly governed by the π electron network of donor and acceptor molecules and the ratio of the number of acceptor molecules to that of the donor molecules, which dominates the filling of a donor π electron band. The first candidate of organic metals is a charge transfer complex, TTF-TCNQ (tetrathiafulvalene-tetracyanoquinodimethane), composed of one-dimensional (1D) independent columns of donor TTF and acceptor TCNQ molecules with the fractional charge transfer of $\delta \approx 0.59$ electron between them. TTF-TCNQ shows a sharp and remarkably large conductivity maxima up to $\sigma \approx 3 \times 10^5$ S/cm around 54 K, which is not superconducting fluctuation, as is initially conjectured [3], but is Peierls transition to an insulating state [4]. The first category of organic superconductors is quasi-one dimensional electronic systems, $(TMTSF)_2X$ (TMTSF = tetramethyltetraselenafulvalene, X = PF_6, AsF_6, ClO_4, etc.) [5] and $(TMTTF)_2Br$ (TMTTF = tetramethyltetrathiafulvalene) with $T_C \approx 1$ K, mostly under pressure. The organic superconductors with the higher transition temperatures up to ≈14 K have been realized with BEDT-TTF donor molecules [bis(ethylenedithio)tetrathiafulvalene, commonly abbreviated with "ET"], which form two dimensional π electron networks [6]. In addition to the superconductivity, the charge transfer salts provide a variety of exotic physical properties by adjusting chemical and physical parameters like chemical modifications of donor and acceptor molecules including molecular symmetry and many crystal phases with the same composition including segregated donor and acceptor stacks and alternately mixed stacks of donor and acceptor molecules. Thus, we are possible to continuously control the structure of the π electron networks from 1D to 2D, the filling of the π electron bands and electron–electron correlation of π bands, resulting in not only non-BCS superconductor, but also metals with variety of ground states like antiferromagnetic (AF), charge density wave (CDW), spin density wave (SDW), spin Peierls (SP), charge ordering (CO) states, and their combinations with exotic magnetic structures, for example, magnetic-field induced superconductivity [7]. Then, STM investigation of these organic systems is useful to collect local information of the π electron systems of the crystal surface layer [1, 8–18].

http://dx.doi.org/10.5772/63406

In this chapter, the STM images in the surface donor layers of the three charge transfer salts, α-(BEDT-TTF)$_2$I$_3$, known as a bulk Dirac Fermion system under pressure [19], β-(BEDT-TTF)$_2$I$_3$ with superconducting transition [20] and (EDO-TTF)$_2$PF$_6$ (EDO–TTF= ethylene dioxy tetrathiafulvalene) with multi-instability around room temperature (RT) [21, 22] are analyzed with the atomic π electron orbitals of sulfur, oxygen and carbon atoms, which are the main carrier of the π electrons. These salts have segregated 2D layers of the BEDT-TTF or EDO-TTF donor molecules and I_3^- or PF_6^- anion molecules. Two (four) donor molecules construct a unit cell with one (two) I_3^- or PF_6^- anion molecule(s); thus, two donor molecules have one electron hole in all the salts [23, 24, 21].

We have deduced three different kinds of surface molecular reconstructions by the electron wavefunction analysis of STM images, as follows.

1. *Charge* redistribution in α-(BEDT-TTF)$_2$I$_3$
2. *Translational* reconstruction up to 0.1 nm in β-(BEDT-TTF)$_2$I$_3$
3. *Rotational* reconstruction transforming the 1D axis from *a* to *b* in (EDO-TTF)$_2$PF$_6$

These surface reconstructions stabilize the π electron system with the additional gain of the cohesive energy in the surface donor layer caused by the removed steric hindrance with the anion molecules of the missing outside double layer.

In α-(BEDT-TTF)$_2$I$_3$, it was found that the electronic states of the surface layer are CO state without definite displacement of the molecules, but with small molecular rotation <1°. This surface state is similar to the CO ground state of the bulk system below 135 K, which would be caused by calming down of the thermal vibration in the end ethylene group of BEDT-TTF molecules. It is suggested that the missing steric hindrance of the surface BEDT-TTF molecules with I_3^- ions of the missing outside double layer stabilizes the ground CO state at 300 K even with thermal vibration of the ethylene groups. In β-(BEDT-TTF)$_2$I$_3$, the translational reconstruction up to ≈0.1 nm along the *a* axis was found in the surface BEDT-TTF layer. This reconstruction removes a staggered structure of the (BEDT-TTF)$_2$ molecular units, resulting in the increase of the cohesive energy between the surface BEDT-TTF molecules. In (EDO-TTF)$_2$PF$_6$, asymmetric EDO-TTF molecules stack with head-to-tail type arrangement, but TTF groups as the main carrier of the π electrons stack without distinctive staggering. The STM image suggests large rotational modifications of the surface EDO-TTF molecules, which drastically modify the electronic structure of the surface layer. The π band of the bulk crystal is one dimensional with a side-by-side single sulfur network along the *a* axis, but that of the surface EDO-TTF layer is along the stacking *b* axis with a face-to-face sulfur pair network, which enhances the cohesive energy and stabilizes the π electron system of the surface EDO-TTF layer.

1.1. Surface states of charge transfer salts

When we proceed with the wavefunction analysis of STM images, it is useful to consider what is the same as and what can be different from that of the interior layers. The charge neutrality

must be kept not only in the whole crystal, but also in each local double layer formed by donor (cation) and acceptor (anion) layers in the segregated layer salts, as in the present salts.

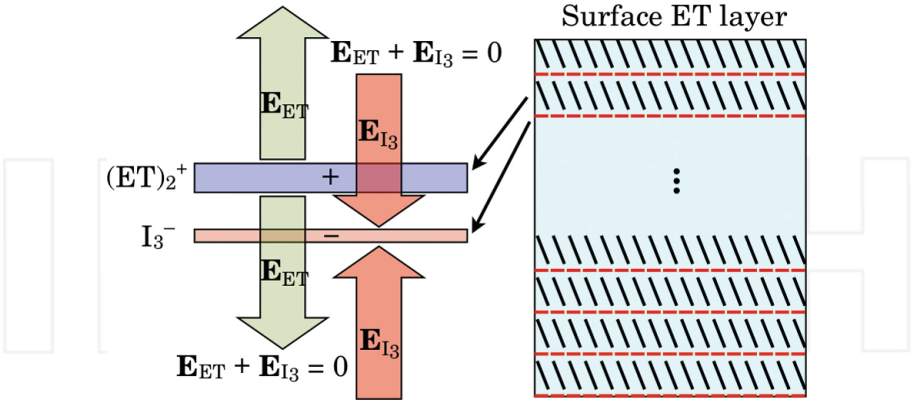

Figure 1. Schematic picture of the electric field produced by a ET_2^+ and I_3^- double layer with the same total charges of each layer in α-(BEDT-TTF)$_2$I$_3$. The electric field of the double layer is confined inside the double layer. That is, outside the double layer, the electric field cancels out. However, the leakage electric field near the double layer forms the electric dipolar field, which binds the neighboring double layers. Thus, the surface ET layer approximately feels only the electric field of the I_3^- layer within the double layer (reused from Ref. [1]).

Figure 1 schematically describes the two-dimensionally stacked structure of the present salts like α-(BEDT-TTF)$_2$I$_3$, in which the total number of $(BEDT\text{-}TTF)_2^+$ layers must be equal to that of I_3^- layers to keep the charge neutrality of the crystal. A set of $(BEDT\text{-}TTF)_2^+$ and I_3^- layers forms an electric double layer like a capacitor, and then, the whole electric field produced by the double layer is confined inside the double layer, as well known in the elementary electrostatics of a capacitor. Then, the electric field outside the double layer is approximately zero and the neighboring double layers are only weakly bound each other by the short-range electric dipolar field leaked locally from the double layers. This fact agrees with the reported experimental finding that the STM probe tip can peel off only the pairs of cation and anion molecules [11]. As in the present salts with the stable anions such as I_3^- and PF_6^-, the total number of the holes in a cation layer must be equal to that of the anions in a double layer independent of the surface layer or the interior layers, which provides the local charge neutrality.

Thus, the reconstructions of a surface layer can happen as charge redistributions and/or structural redistributions, keeping the charge neutrality of each double layer. Next, we focus on the Coulomb forces exerted on a cation layer by anion layers hereafter.

On the Coulomb forces exerted to the surface cation layer by the interior layers, it is useful to separate the cases:

1. Inside double layers, and

2. The partner anion layer of the surface double layer.

On the first point, since the electric field is absent outside the double layer, the long-range Coulomb force of the inside double layers does not exist, as mentioned above. On the second point, the partner anion layer of the double layer generally forms a flat sheet and generates approximately uniform electric field normal to the anion layer [1]. The uniform electric field attracts uniformly the cation layer sheet, in which the cation molecules are tightly bound each other by the cohesive interaction with the other cation molecules, forming a π band, under constraint of the steric hindrance with the cation molecules and the partner anion molecules in the double layer. This situation is the same as that for all the double layers and there is no special situation even in the surface layer. Only the difference of the surface double layer from the inside is that the short-range dipolar electric field by a missing double layer outside is absent, which affects only limitedly to the attraction between the members of the double layer because of its short-range nature of the dipolar field.

Thus, the Coulomb interaction between the cation and the anion layer of the electric double layer does not the main origin of the structural reconstruction in the surface ET layer, but the unique origin of the structural reconstruction can be the missing steric hindrance with the anion layer of the missing outside double layer, which competes with the cohesive interaction within the surface cation layer.

2. Wavefunction analysis

The analysis of STM images with atomic wavefunctions is described for α-(BEDT-TTF)$_2$I$_3$, as an example of the organic charge transfer salts, where the cohesion is dominated by the van der Waals interaction and the π electron transfer integrals. **Figure 2** shows a schematic picture of the surface layer of the flat donor molecules with the π wavefunctions of the end sulfur atoms, and the STM probe tip with the s wavefunction. An STM topography $\Delta h(x)$ in a constant current mode is obtained by controlling the height of the probe tip to keep the tunneling current constant with scanning the probe tip. The higher the probe tip, the brighter the topography appears. The topography is simulated by a constant amplitude contour of the π wavefunctions, $\Psi(\Delta h, x)$ along the scan direction x parallel to the plane of the donor layer.

The unit cell of α-(BEDT-TTF)$_2$I$_3$ contains four BEDT-TTF molecules (express by ET, hereafter), labeled by A, A′, B, and C with different π charge numbers by charge disproportionation (CD) caused by the anisotropic transfer integrals between the molecules in the unit cell. The wavefunction Ψ^i_{S3p} for the $3p$ orbital of the relevant sulfur atom in the ET(i) molecule (i = A, A′, B and C) is expressed as

$$\Psi^i_{S3p} = \sqrt{\rho_i f_S}\Psi_{S3p}, \tag{1}$$

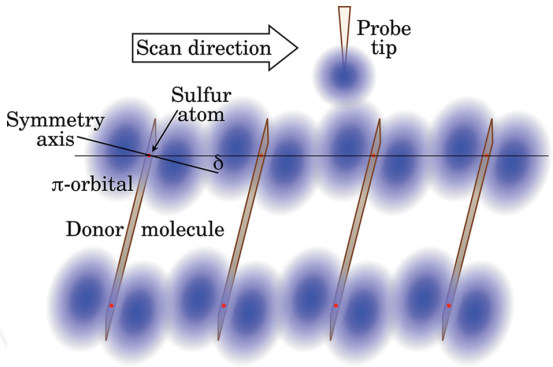

Figure 2. A schematic picture of a donor layer with a flat molecular plane. Electron wavefunctions are described by blue ellipses for π electrons of the donor molecules and a blue circle for s electron of the probe tip. The symmetry axis of the π orbital is perpendicular to the molecular plane, which leans by δ to the plane of the donor layer expressed by the thin solid horizontal line through the sulfur atom.

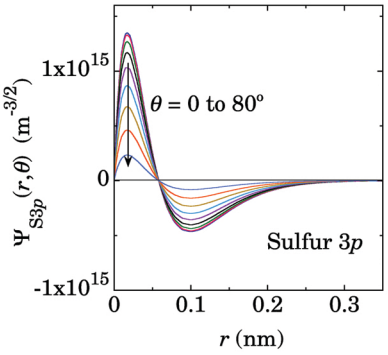

Figure 3. $3p$ wavefunction of a sulfur atom with the effective nuclear charge of $Z_{eff} = 5.48$ for every 10° of θ from 0 to 80, which is defined in **Figure 4**. r is the distance from the sulfur nucleus. STM usually observes the region much farther than 0.1 nm (reused from Ref. [1]).

where ρ_i is the number of π charges in the highest occupied molecular orbital (HOMO) band of each ET(i) molecule, f_S is the fraction of π charges at the sulfur atom in each ET(i) molecule, and Ψ_{S3p}, as shown in **Figure 3**, is the wavefunction of the sulfur $3p_\pi$ orbital with the atomic number $Z = 16$, expressed as

$$\Psi_{S3p} = \sqrt{\frac{2}{\pi}\left(\frac{Z_{\text{eff}}}{a_0}\right)^5}\,\frac{r}{81}\left(6 - \frac{Z_{\text{eff}}r}{a_0}\right)\exp\left(-\frac{Z_{\text{eff}}r}{3a_0}\right)\cos\theta, \tag{2}$$

and for $2p_\pi$ orbitals,

http://dx.doi.org/10.5772/63406

$$\Psi_{2p} = \sqrt{\frac{1}{2\pi}\left(\frac{Z_{\text{eff}}}{a_0}\right)^5}\,\frac{r}{4}\exp\left(-\frac{Z_{\text{eff}}r}{2a_0}\right)\cos\theta, \tag{3}$$

where $a_0 = 5.29 \times 10^{-11}$ m is the Bohr radius, and $Z_{\text{eff}} = 5.48$, 4.45, and 3.14 is the effective nuclear charge for the sulfur, oxygen, and carbon, respectively, in which the screening effect of the inner core electrons is taken into account [25]. The representative contour of the constant Ψ_{S3p} is shown in **Figure 4**. The tunnel current I in the limits of small voltage and low temperature is expressed as [26]

$$I_{\text{tunnel}} = \left(\frac{2\pi}{\hbar}\right) e^2 V_a \Sigma_i \left|M_{\mu,i}\right|^2 \delta(E_i - E_{\text{F}})\delta(E_\mu - E_{\text{F}}), \tag{4}$$

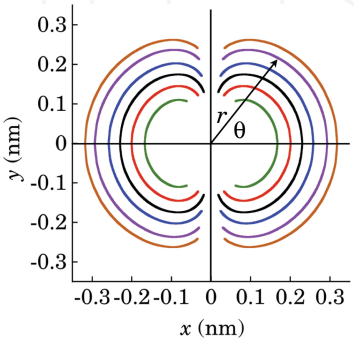

Figure 4. Constant amplitude contour of 3*p* wavefunction of a sulfur atom deduced from **Figure 3** for the STM topography analysis in α-$(ET)_2I_3$. The abscissa corresponds to the symmetry axis of the 3*p* orbital of the sulfur atom at the origin, perpendicular to the molecular plane corresponding to the vertical line. Each constant amplitude of $|\Psi_{S3p}|$ is 5×10^{12}, 1×10^{13}, 5×10^{13}, 1×10^{14}, and $2\times10^{14} m^{-3/2}$ from the outer to the inner (reused from Ref. [1]).

where V_a is the applied voltage; $M_{\mu,i}$ is the tunneling matrix element between the Ψ_μ of the probe tip and Ψ^i_{S3p} of the relevant sulfur atom; and E_i, E_μ, and E_{F} are the energies of the states Ψ^i_{S3p} and Ψ_μ in the absence of tunneling, and the Fermi energy of the tip, respectively. The matrix element is expressed as

$$M_{\mu,i} = -\left(\frac{\hbar^2}{2m}\right)\int dS \cdot (\Psi^*_\mu \nabla\Psi^i_{S3p} - \Psi^i_{S3p}\nabla\Psi^*_\mu), \tag{5}$$

where the integral is over any surface lying entirely within the barrier region. The probe wavefunction Ψ_μ is taken to be independent of ET(i). In the constant current mode, the difference of Ψ^i_{S3p} produces the probe height change Δh, which depends on the local density of states proportional to $\rho_i f_s$ under the constant tunneling current condition.

Thus, the observed topography can be simulated with the adjustable parameter of ρ_i providing f_S is independent of the sites. The relative fraction of ρ_i on the ET(i) site is related to the amplitude of the sulfur 3p wavefunction $\Psi_{S3p}(r_i^{max})$, where r_i^{max} is the radial distance from the relevant sulfur nucleus of ET(i), where the tip height is maximum. The condition for providing the same tip current at each maximum tip height is expressed as

$$\Psi^i_{S3p}(r_i^{max}) = \Psi^j_{S3p}(r_j^{max}),$$
$$\frac{\Psi^i_{S3p}(r_i^{max})}{\Psi^j_{S3p}(r_j^{max})} = \sqrt{\frac{\rho_i}{\rho_j}}\,\frac{\Psi_{S3p}(r_i^{max})}{\Psi_{S3p}(r_j^{max})} = 1. \quad (6)$$

Thus, the ratio of the charge number in ET(i) to ET(j) can be described in terms of the amplitude of Ψ_{S3p} as

$$\frac{\rho_i}{\rho_j} = \left(\frac{\Psi_{S3p}(r_j^{max})}{\Psi_{S3p}(r_i^{max})}\right)^2. \quad (7)$$

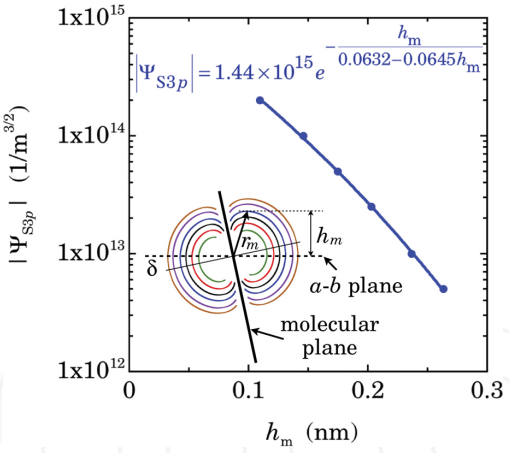

Figure 5. Maximum height h_m estimated from each Ψ_{S3p} wavefunction contour in the inset, where the symmetry axis (thin solid line) of the 3p wavefunction tilts by $\delta \approx 12$ deg against the a–b plane described by the dashed horizontal line through the sulfur atom. The analytical expression approximately describes $|\Psi_{S3p}|$ as a function of h_m, which is applicable to the STM topography analysis in the a–b plane of α-$(ET)_2I_3$ (reused from Ref. [1]).

Figure 5 shows a more realistic configuration of h_m with a tilting angle of $\delta = 12°$ for $\Psi_{S3p}(h_m)$ in α-$(ET)_2I_3$, where h_m is the maximum height of the contour curve measured from the relevant sulfur atom, as shown in the inset. Since $\Psi_{S3p}(h_m)$ decays exponentially, the following phenomenological formula is derived to reproduce the data:

$$\left|\Psi_{S3p}\right| = a\exp\left(-\frac{h_m}{h_0}\right) = a\exp\left(-\frac{h_m}{b-ch_m}\right). \tag{8}$$

Figure 5 demonstrates that the data points around $h_m \approx 0.2$ nm are represented well by the parameters $a = 1.44 \times 10^{15}$ m$^{-\frac{3}{2}}$, and the correlation length $h_0 = b - ch_m$ nm, where $b = 0.0632$ nm and $c = 0.0645$. Thus, the molecular charge ratio of ET(i) to ET(B) is described with the relative difference $\Delta h_{m,i}$ by

$$\begin{aligned}\frac{\rho_i}{\rho_B} &= \left(\frac{\Psi_{S3p}(h_{m,B})}{\Psi_{S3p}(h_{m,B}+\Delta h_{m,i})}\right)^2 \\ &= \exp\left\{-2\left(\frac{h_{m,B}}{b-ch_{m,B}} - \frac{h_{m,B}+\Delta h_{m,i}}{b-c(h_{m,B}+\Delta h_{m,i})}\right)\right\},\end{aligned} \tag{9}$$

where $h_{m,B}$ is the maximum height for ET(B) and $h_{m,i} = h_{m,B} + \Delta h_{m,i}$ for ET(i). $\Delta h_{m,i}$ can be directly measured as Δh_i for each ET(i); the tip height difference from ET(B) with some corrections is described in **Table 1** in the next section.

						Case (a)		Case (b)	
	Δh_i	$h_{m,i}$	$\Delta_{S,i}$	δ_i(deg)	$\Delta_{\delta,i}$	Δ_{CD_i}	$\Delta h_{ap,i}$	$\Delta h_{m,i}$	ρ_i / ρ_B
B	0	0.23	0	10.4	0	0	0	0	1
C	−0.025(7)	0.21	−0.003	12.9	−0.003	−0.007	−0.012	−0.019	0.36
A	−0.012(7)	0.22	0.000	11.3	−0.003	−0.003	−0.006	−0.009	0.61
A′	−0.022(7)	0.21	−0.002	11.2	−0.002	−0.003	−0.015	−0.018	0.38

Table 1. Tip height difference Δh_i measured by STM topography relative to ET(B) from **Figure 10** for α-(BEDT-TTF)$_2$I$_3$. $h_{m,i}$ is estimated from the simulation of the topographies and is utilized to estimate $\Delta_{\delta,i}$. $\Delta_{S,i}$ is the relative height difference of the relevant sulfur atom to ET(B) measured from the a–b plane, extracted from the structural data [23]. δ_i represents the angle of 3p orbital axis against the $a - b$ plane and $\Delta_{\delta,i}$ is the relative height change caused by δ_i, which is proportional to $h_{m,i} \cdot \Delta_{CD_i}$ is the expected tip height due to the charge distribution caused by the CD state at RT and $\Delta h_{m,i} = \Delta h_i - \Delta_{S,i} - \Delta_{\delta,i}$ is the apparent change caused by the surface reconstruction over the CD state in the case (a). $\Delta h_{m,i} = \Delta h_i - \Delta_{S,i} - \Delta_{\delta,i}$ is the experimental relative height in the case (b), which gives the ratio of molecular charge with respect to ET(B), that is, ρ_i / ρ_B. All the length scales are in nm (reused from Ref. [1]).

3. Surface reconstruction in charge transfer salts

3.1. Charge redistribution in α-(BEDT-TTF)$_2$I$_3$

Figure 6 shows the crystal structure of α-(ET)$_2$I$_3$ in the a–b plane and relative locations of I_3^- ions in (B). The electrical property of the bulk crystal is conductive above 135 K and the charge

ordered insulating state below 135 K. The unit cell contains four ET molecules and three non-equivalent sites (A, A′), B and C at RT with different charges of the CD state. **Figure 7** shows the molecular structure of ET with HOMO molecular orbitals calculated by MOPAC. The π electrons are mainly located on the TTF group and partially on the "dithio" sulfur atoms, but not on the ethylene group. As a result, the π charge fraction on the end "dithio" sulfur atom(s) is observed by STM in the *a*–*b* plane.

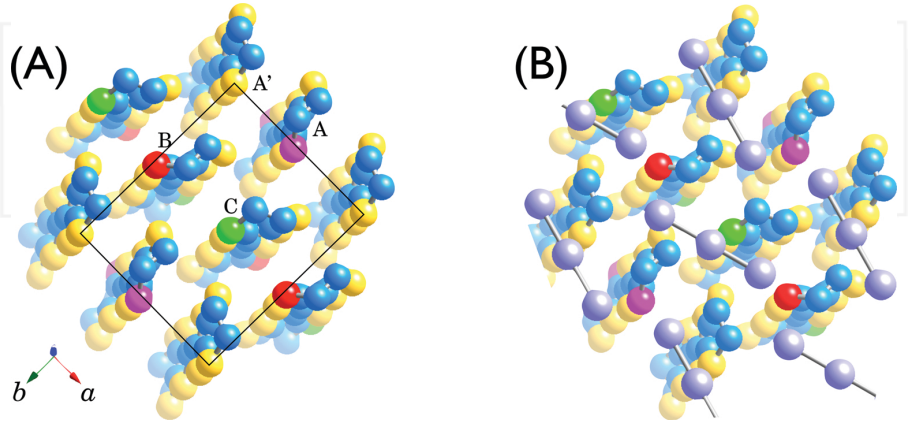

Figure 6. Unit cell structure of α-$(ET)_2I_3$ determined by the X-ray analysis at 300 K [23]. Blue and yellow balls indicate carbon and sulfur atoms, respectively. Hydrogen atoms are not indicated. The labels A, A′, B, and C show the four molecules in a unit cell. The sulfur atoms observed by STM are marked by the special colors of purple, yellow, red and green for A, A′, B, and C molecules, respectively. a = 0.9187 nm, b = 1.0793 nm, c = 1.7400 nm, α = 96.957°, β = 97.911°, and γ = 90.795°. (B) shows relative location of I_3^- ions.

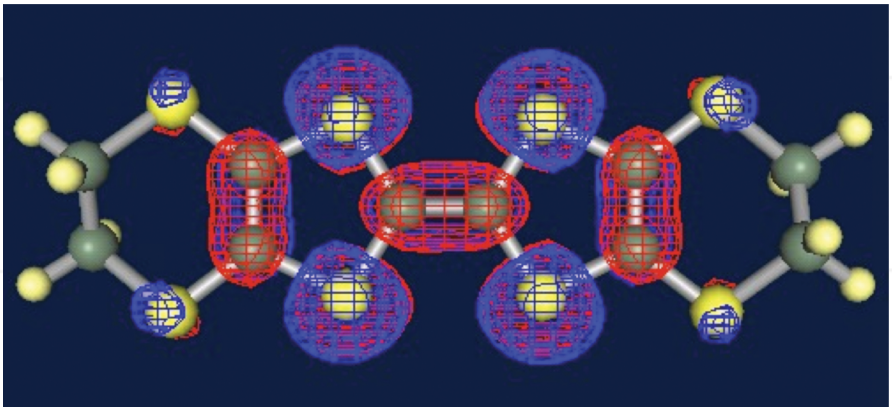

Figure 7. Molecular structure of BEDT-TTF with HOMO molecular orbitals of π electrons calculated by MOPAC. The size of the orbitals represents the relative fraction of HOMO electrons (reused from Ref. [1]).

http://dx.doi.org/10.5772/63406

STM was carried out at RT with easyScan 2 (NanoSurf®). A mechanically sharpened $Pt_{0.8}Ir_{0.2}$ wire, the constant tunneling current (setpoint) of 1 nA and tip potential of 10 mV were used. The α-$(ET)_2I_3$ samples typically with 5 × 2 × 0.05 mm^3 were prepared following a previously reported procedure [27]. The SPIP image processing software is utilized to eliminate instrumental drift of STM on the basis of the reported lattice parameters [23].

3.1.1. Site assignment

The charge distribution in the surface $(ET)_2$ layer is analyzed with the wavefunction analysis described in the previous section [1]. **Figures 8** and **9** show the observed STM images in the *a*–*b* plane, where the higher the probe tip, the brighter the topography appears. There are two characteristic points in these images: absence of a noticeable long-range modulation and the periodic characteristic structure made of four types of brightness and shapes. These are helpful features to assign the crystal structure. The *a* axis along ET(A)–ET(A′) and ET(B)–ET(C) is assigned to run from the top left to the bottom right. The brightest areas are assigned to the ET(B) because of the largest molecular charge at RT, as cited in **Table 2** [23]. Then, the less bright areas in the same arrays as ET(B) are assigned to ET(C). The other arrays with small and less bright areas in between the ET(B)–ET(C) arrays correspond to the ET(A)–ET(A′) arrays. Although the charge numbers of ET(A) and ET(A′) are equivalent to each other at RT in the bulk crystal [23], the observed brightness of the ET(A)–ET(A′) arrays of the surface layer suggests some non-equivalence of the alternate brightness.

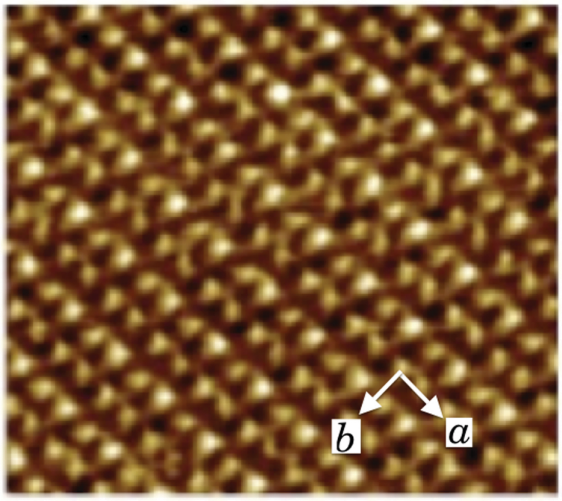

Figure 8. STM image of a thin plate-like single crystal of α-$(BEDT\text{-}TTF)_2I_3$ in ≈ 7.0 × 6.5 nm^2, where the thermal drift was corrected with the reported lattice parameters [23]. The assigned *a* and *b* axes are indicated by the arrows (reused from Ref. [1]).

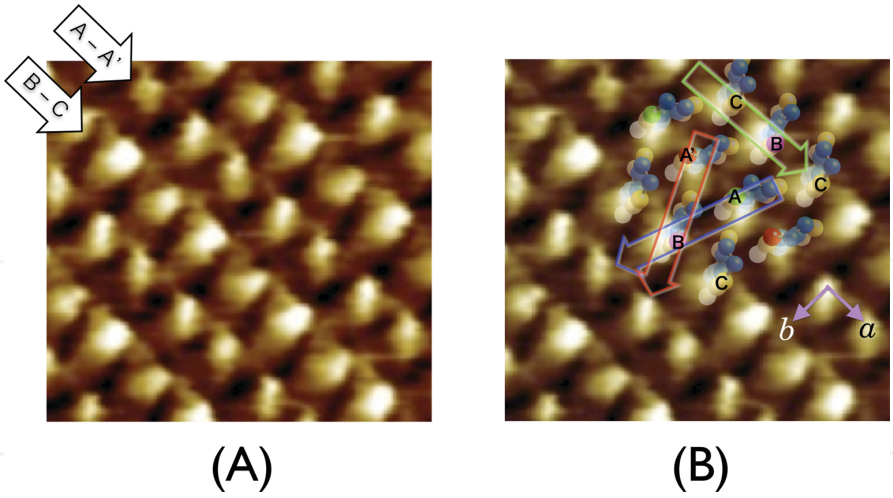

Figure 9. STM image of α-(BEDT-TTF)$_2$I$_3$ in 2.8 × 2.6.nm^2. Four BEDT-TTF molecules are contained in the unit cell. (A) Molecular arrays, A–A′ and B–C, run from the top left to the right bottom. (B) Crystal structure assigned to the STM image of α-(BEDT-TTF)$_2$I$_3$. The balls with A′, A, B, and C represent the relevant sulfur atoms. The three large arrows represent the direction of the topography shown in **Figure 10** (reused from Ref. [1]).

Site	Present results	X-ray results	
	RT	RT	20 K
B	0.42(8)	0.29(2)	0.35(4)
C	0.16(2)	0.21(3)	0.12(5)
A	0.26(5)	0.25(2)	0.39(5)
A′	0.16(2)	0.25(2)	0.14(5)

Table 2. Relative molecular charge $\rho_i / \sum_i \rho_i$ for α-(BEDT-TTF)$_2$I$_3$ in the case (b), which is compared with that estimated by X-ray analysis [23]. Note the broken inversion symmetry between ET(A) and ET(A′), which suggests the rich charge stripes of the B-A-B type. The parentheses show uncertainty in the last digit (reused from Ref. [1]).

Figure 9B shows the STM image with the structure determined by X-ray analysis [23], where the position and direction of the bright areas agree with the 3*p* orbitals of the sulfur atoms without recognizable reconstructions. Here, note that the halves of the sulfur 3*p* orbitals on the single side of the molecular plane are observed in the image because of the tilted symmetry axis of the sulfur 3*p* orbital by ≈12° out of the *a*–*b* plane.

Figure 10 shows the several superposed topographies along with the three arrow directions of **Figure 9B**, which enables us to average the random error out graphically to estimate the probe height difference Δh_i relative to ET(B). Several parameters derived from Δh_i are summarized in **Table 1**. The characteristic features of the topographies are as follows.

- $\Delta h_A'$ is almost the same as Δh_C, and Δh_A appears in between Δh_B and $\Delta h_A'$ or Δh_C, suggesting symmetry breaking between ET(A) and ET(A′) in the surface ET layer.
- Both steep changes related to the nodes of 3*p* wavefunctions and long tails caused by overlapping of the wavefunctions are found.

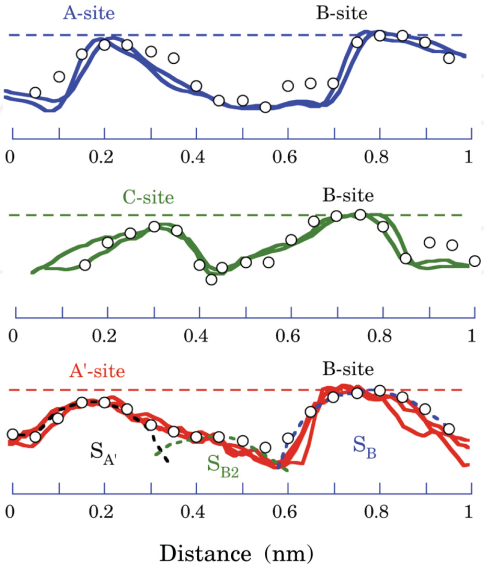

Figure 10. STM topographies of α-(BEDT-TTF)$_2$I$_3$ (solid curves) and the simulations (open circles) with $\Sigma_i \mid \Psi^i_{S3p} \mid^2$, where the molecular charge ratio ρ_i / ρ_B in **Table 1** was taken into account. The topographies were measured along the arrows in **Figure 9(B)**. The horizontal dashed straight lines are visual guides at the top of the S_B site. The broken curves for the bottom A–B scan show individual contributions of each sulfur atom at S_B and $S_{A'}$ and S_{B2}. From S_B, note that S_{B2} is 0.1 nm inside. The vertical scale is the same as the horizontal one (reused from Ref. [1]).

Several interpretations on the surface states in comparison with the bulk states are possible:

1. Molecular reconstruction [case (a)]
2. Molecular charge redistribution [case (b)]
3. Molecular reconstruction with charge redistribution [case (c)].

In the following sections, the possibilities of the structural and the charge redistribution are considered.

3.1.2. Structural reconstruction

It is informative to know how the structural parameters change across the phase transition at 135 K from the CD state to the CO state in the bulk system. A remarkable molecular charge redistribution has occurred across the phase transition from nearly equivalent charges within

the unit cell at RT to the rich and the poor charge stripes below 135 K. It is a crucial point that the displacement perpendicular to the *a*–*b* plane is remarkably small around 0.001 nm or less with the molecular rotation as small as 0.75°, which corresponds to a 0.002 nm change in the position of the relevant sulfur atom perpendicular to the *a*–*b* plane [23]. A possibility of the small molecular rotation of the order of 0.75° is not rejected, but the effect to the brightness and the shapes of the STM image would be negligibly small in the present wavefunction analysis. Thus, these facts and the consideration in Section 1.1 strongly suggest that the possibility of the structural reconstruction perpendicular to the *a*–*b* plane, which is sensitive to the estimation of the charge redistribution, would not be realistic in α-$(ET)_2I_3$.

3.1.3. Charge redistribution

In this section, the most probable case (b) is discussed; the observed Δh_i's are caused by the charge redistribution in the unit cell. In **Figure 10**, the calculated contour profiles of $\Sigma_i \mid \Psi^i_{S3p} \mid^2$ are shown for the tunneling current. Here, it is demonstrated that the sulfur 3*p* wavefunctions reproduce the characteristic features of the topographies well. The nodes of the 3*p* wavefunctions produce the steep changes near the sulfur atoms. In contrast, overlap between the neighboring S_{3p} wavefunctions reproduces the longer tails of the topographies. Particularly, the presence of the second sulfur atom ET(B2) below 0.1 nm from ET(B) is essential along the A′–B direction.

Table 1 shows the ratios of the molecular charges ρ_i/ρ_B in the case (b). **Table 2** demonstrates the fraction of the molecular charge $\rho_i/\Sigma_i\rho_i$ in the unit cell, which can be compared with the reported results [23] derived with an empirical method [28] both at RT and 20 K for the crystal of α-$(ET)_2I_3$. The charge number of ET(A) is equal to that of ET(A′) in the CD state of the bulk crystal at RT, but the charge equivalence of ET(A) and ET(A′) is completely missing in the surface layer; the fraction in ET(A′) is nearly equal to ET(C), which is similar to the CO state at 20 K in the bulk crystal. Thus, it is demonstrated that the CD state at RT is unstable, but the charge redistribution similar to the CO ground state below 135 K is stabilized in the surface ET layer. This difference from the electronic states of the bulk system can be ascribed to a small-angle molecular rotation up to only 0.75° even at RT in the surface layer, where there is no steric hindrance with the missing outside double layer.

In conclusion, the charge redistribution in the surface ET layer, which is similar to the most stable ground state of the CO state below 135 K in the bulk α-$(ET)_2I_3$, is realized by the absence of the constrained steric interaction between the thermal vibration of the ethylene groups of ET molecules and the I_3^- anion layer in the missing outside double layer. This conclusion helps to interpret the mechanism of the CO phase transition at 135 K in the bulk α-$(ET)_2I_3$ crystal as the thermal vibration of ethylene groups, which prevents the inside $(ET)_2$ layers from forming the ground state molecular conformation at RT. Since the thermal vibration ceases around 135 K, the phase transition from the metallic CD state at RT to the insulating CO state in α-$(ET)_2I_3$ crystals is attained. This would be found in the other organic layered systems, such as β-$(ET)_2PF_6$ [8] and θ-$(ET)_2RbZn(SCN)$ [18].

http://dx.doi.org/10.5772/63406

3.2. Translational reconstruction in β-(BEDT-TTF)$_2$I$_3$

The crystal structure of β-(ET)$_2$I$_3$ is triclinic with $(ET)_2^+$ and I_3^- in the unit cell, as shown in **Figure 11**, with a nearly isotropic two-dimensional Fermi surface. The electrical property is metallic with the conductivity of ≈ 30 S/cm at RT [24] and is superconducting at ambient pressure below 1.5 K [20] and 7.4 K under 1.3 kbar [29]. On the basis of the analyzed result of α-(ET)$_2$I$_3$ in the previous section, the missing steric hindrance of the surface (ET)$_2$ layer with the I_3^- layer is also expected to have some effects on the electronic states of the surface (ET)$_2$ layer in β-(ET)$_2$I$_3$. Fortunately, the obtained STM image of β-(ET)$_2$I$_3$ with the setpoint of 1 nA and the tip potential of 10 mV makes us possible to analyze qualitatively the surface reconstruction, as shown in **Figure 12**.

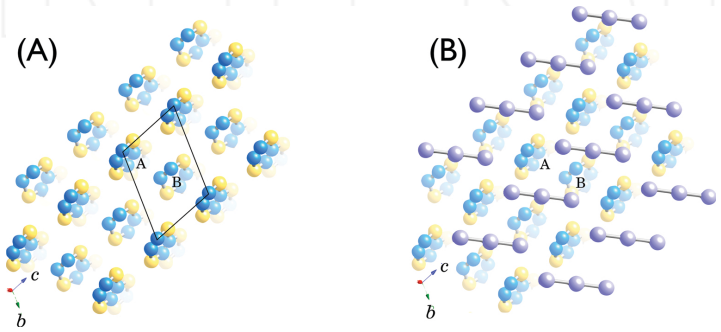

Figure 11. Crystal structure of β-(ET)$_2$I$_3$ in the b–c plane at RT [24]. Crystal data are triclinic with a = 15.243, b = 9.070, c = 6.597 Å, α = 109.73, β = 95.56, γ = 94.32°. Blue and yellow balls indicate carbon and sulfur atoms, respectively. Hydrogen atoms are not indicated. The unit cell contains two ET molecules, ET(A) and ET(B), and one I_3^- ion. (B) shows relative location of I_3^- ions against ET molecules. Note that the steric hindrance of the I_3^- ions with ET(B) is stronger than with ET(A) in this surface and vice versa in the next layer of I_3^- ions.

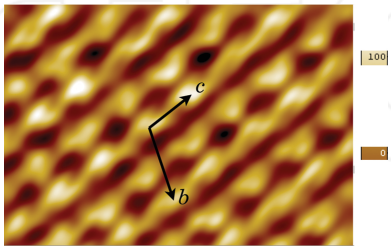

Figure 12. STM image of a needle-like single crystal (0.1 × 0.1 × 3 mm^3) of β-(ET)$_2$I$_3$ in 4.2×2.9 nm^2. Thermal drift was corrected with reference to the reported crystal structure [24], and FFT (fast Fourier transformation) filter was applied. The assigned b and c axes are indicated by the arrows. Note that the two molecules in a unit cell show similar brightness. The brightness reference is shown in the right-hand side (100–0 pm reference).

Figure 13 shows the crystal structure of β-$(ET)_2I_3$ projected along the c axis, which demonstrates the definite difference between ET(A) and ET(B) in the vertical location from the b–c plane. If the surface $(ET)_2$ layer takes the same arrangement as that in the crystal, the remarkable difference of the brightness corresponding to ET(A) and ET(B) is expected in the STM image, but it is not the case. The brightness of the two arrays along the c axis looks almost the same as each other within the uncertainty. Thus, it is concluded that the surface reconstruction is occurred in the $(ET)_2$ surface layer of β-$(ET)_2I_3$.

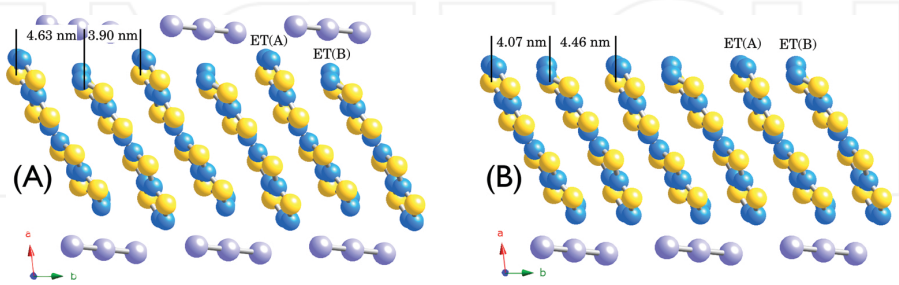

Figure 13. (A) Crystal structure of β-$(ET)_2I_3$ projected along the c axis with three unit cells. ET(A) is located nearer to the b–c surface by ≈ 0.1 nm than ET(B). (B) A model for the surface layer of β-$(ET)_2I_3$. ET(B)s are slid to align TTF double bonds to the same height as that of ET(A), which increases the cohesive energy in the surface ET layer. The separations between ET(A) and ET(B) are contrasted to (A). The topmost sulfur atoms of ET(B) are slightly deeper by 0.01 nm than ET(A).

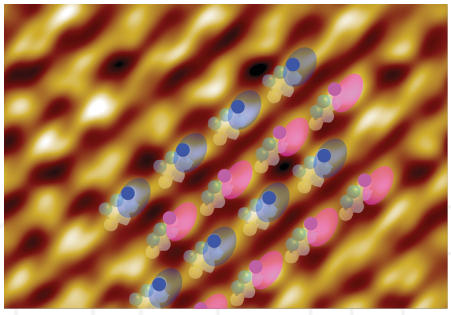

Figure 14. STM image in the b–c plane overlaid by the reconstructed structure with the π clouds. Balls and ellipses indicate the topmost sulfur atoms and the schematic π clouds, respectively. Pink corresponds to ET(A) and blue does ET(B). The difference in the relative location of the π clouds to the sulfur atoms is caused by the difference of the lean angle δ in **Figure 2**.

The origin of the reconstruction is ascribed to the presence of the open space for the surface ET(B) molecules by the missing outside double layer. Thus, the ET molecules in the surface layer are naturally reconstructed to gain additional cohesive energy by relieving the staggered arrangement of ET(A) and ET(B) in the unit cell. In contrast, it is not realistic to ascribe the origin only to some charge redistribution, which must reach three times larger π electron

http://dx.doi.org/10.5772/63406

density in ET(B) compared with that in ET(A) to compensate the difference of 0.1 nm in depth from **Figure 5**. Thus, the most probable origin is the structural reconstruction of the two molecules in the unit cell to align to the same height as each other, which gives a similar brightness of ET(B) to ET(A) in the surface layer of β-$(ET)_2I_3$. Such a structural reconstruction increases the cohesive energy of the surface ET molecular layer with larger π band width and electrical conductivity. The short intermolecular sulfur-to-sulfur contacts are decreased down to 3.09, 3.43 Å in the surface layer in **Figure 13B** from 3.57, 3.58 Å in the bulk crystal [24] in **Figure 13A**. However, since the shortest 3.09 Å in **Figure 13B** looks unrealistically short, some optimization of the molecular arrangement would be required. The simulated surface molecular arrangement in the *b*–*c* plane is overlaid to the STM image in **Figure 14** and reasonably reproduces it, which supports the model of the structural reconstruction in the surface ET layer of β-$(ET)_2I_3$.

3.3. Rotational reconstruction in $(EDO\text{-}TTF)_2PF_6$

The electronic states of $(EDO\text{-}TTF)_2PF_6$ are of 1D metal along the *a* axis at RT with internal multi-instability and are transformed to charge ordered insulating states below 280 K associated with distinctive molecular deformations [22]. The mechanism of the metal-insulator transition is interpreted as the cooperation of Peierls instability, charge ordering, and the order–disorder transition of the countercomponent. The crystal structure projected in the *a*–*b* plane is shown in **Figure 15**. The unit cell of $(EDO\text{-}TTF)_2PF_6$ contains $(EDO\text{-}TTF)_2$ and PF_6. The structure of EDO-TTF molecule is shown in **Figure 16** together with the molecular orbital of π electrons. EDO-TTF molecules stack along the *b* axis with head-to-tail type arrangement, as described in **Figure 17**.

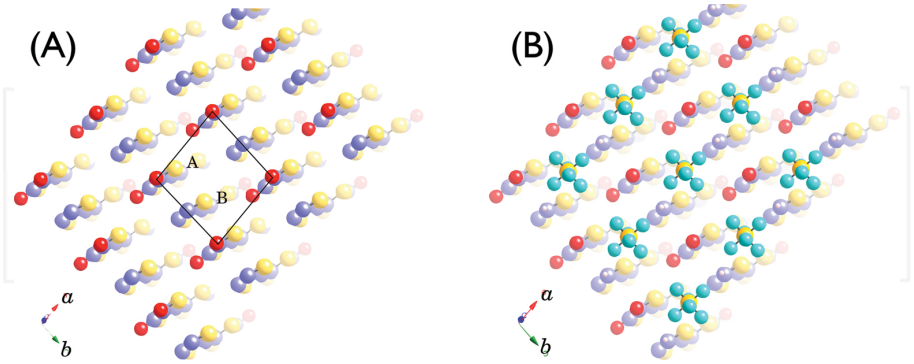

Figure 15. Structure of $(EDO\text{-}TTF)_2PF_6$ at RT [21]. Crystal data are triclinic with a = 7.197, b = 7.343, c = 11.948 Å, α = 93.454, β = 75.158, γ = 97.405°. Blue, yellow, and red balls indicate carbon, sulfur, and oxygen atoms, respectively. Hydrogen atoms are not indicated. The unit cell contains two EDO-TTF molecules and one PF_6^- ion. (B) shows relative location of PF_6^- ions to EDO-TTF molecules.

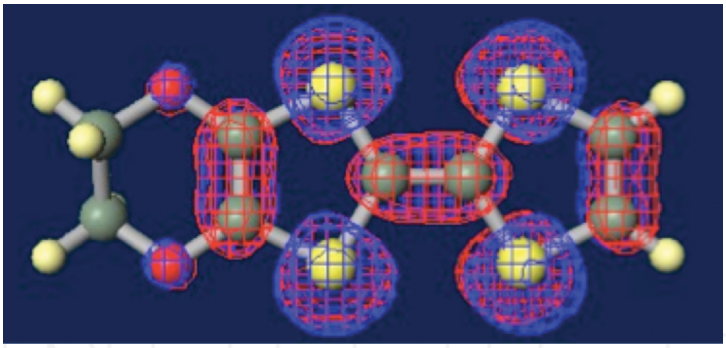

Figure 16. Molecular structure of EDO-TTF with HOMO molecular orbitals of π electrons calculated by MOPAC. The size of the orbitals represents the relative fraction of HOMO electrons. The oxygen sites contain a limited density of π electrons compared with that in the carbon sites.

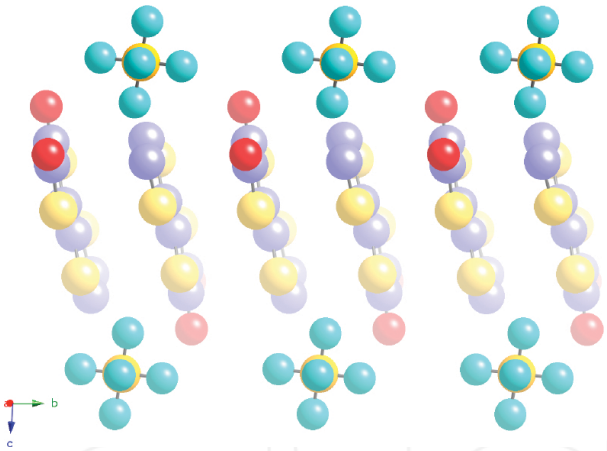

Figure 17. Crystal structure of $(EDO\text{-}TTF)_2PF_6$ along the direction perpendicular to the *b*–*c* plane. PF_6 has no serious steric hindrance with the EDO-TTF layers.

The single crystals of $(EDO\text{-}TTF)_2PF_6$ with needle like thin plate ($1.0 \times 3.0 \times 0.5$ mm^3) are used for STM study and are too brittle to pass through the transition temperature at 280 K. Thus, STM data were obtained only at RT. The image of $(EDO\text{-}TTF)_2PF_6$ in **Figure 18** was taken in the *a*–*b* plane with the setpoint of $I = 6.1$ pA and the tip potential of $V_{tip} = 200$ mV. The whole image is periodically filled by the characteristic structure with different brightness and sized areas in each unit cell. The *a* axis was assigned as the direction, in which the profiles without distinctive structure are arrayed. In contrast, some structure caused by the head-to-tail array is expected along the *b* axis. No superstructure over multiple unit cells is found.

http://dx.doi.org/10.5772/63406

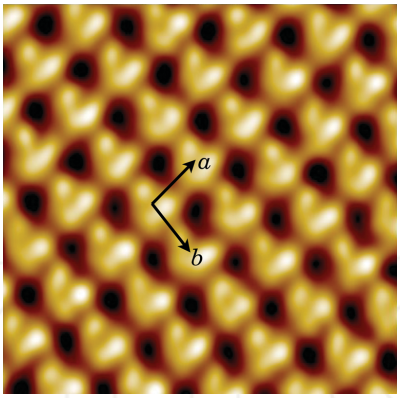

Figure 18. STM image of a single crystal of $(EDO\text{-}TTF)_2PF_6$ in 4.7 × 4.7 nm^2 with the setpoint of 6.1 pA and the tip potential of 200 mV. Thermal drift was corrected with reference to the reported crystal structure [21] and FFT filter was applied. The assigned *a* and *b* axes are shown by the arrows.

Although the EDO-TTF molecules stack with the head-to-tail type arrangement, but the main π electron carriers of TTF groups stack without distinctive staggering. As a result, there would be no motive force for the surface EDO-TTF molecules to adjust their height by sliding along the molecular plane even with the open space of the missing outside double layer, as in the case of β-$(ET)_2I_3$ in Section 3.2.

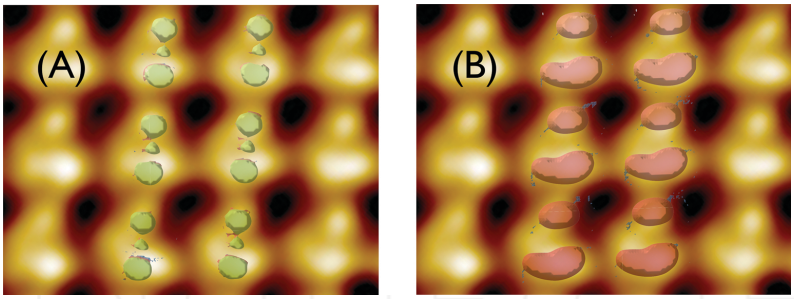

Figure 19. STM image of $(EDO\text{-}TTF)_2PF_6$ with (A) the simulated constant charge density contour of 3 × 10^{-8} nm^{-3} at 2 Å from the oxygen atom. The second oxygen and the second carbon contribute only a little. The small spots are assigned to the second half of O_{2p} orbital and with (B) the simulation by the rotational reconstruction model with the condition of $\theta_a = 18°$, $\theta_b = 29°$ as described in **Figure 20**, which successfully reproduces the overall profile of the observed image.

The analysis with O_{2p} and C_{2p} wavefunctions is applied to $(EDO\text{-}TTF)_2PF_6$ system. With the ratio of the π charges of the oxygen site to the carbon site, 0.149:0.358 estimated by MOPAC, the constant amplitude contour of the π charge density of 3 × 10^{-8} nm^{-3} at 2Å from the oxygen atom is compared with the STM image in **Figure 19(A)**. The large and wide bright areas are assigned to the oxygen atoms of EDO groups and the smaller ones are attributed to the carbon atoms of TTF groups. If the simulated contours of the carbon atoms in the TTF end are located

on the center of the small areas in **Figure 19(A)**, the simulated contours of the oxygen atoms in the EDO groups show only rough agreement with the STM image, but clearly deviates from the brightest centers at the right-hand side of the large areas in **Figure 19(A)**. The second half of O_{2p} orbital in the simulation is also missing in the STM image. These deviations suggest the presence of some modification in the arrangement of EDO-TTF molecules in the surface layer.

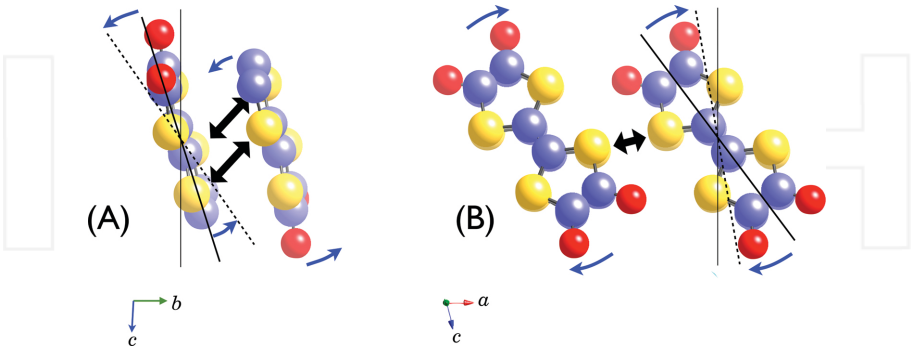

Figure 20. Possible reorientation in the surface EDO-TTF layer. (A) Rotation about the axis parallel with the molecular plane and the *a*–*b* plane to lay them down in the *a*–*b* plane. For simplicity, the *a* axis is used. (B) Rotation about the normal to the molecular plane to raise them. In actual, the *b* axis is used. The black arrows indicate the π electron network (A) along the *b* axis with the double pathways and (B) along the *a* axis with the single pathway.

The possible reconstruction consistent with the STM image is rotational reconstruction as follows and as described in **Figure 20**.

1. Lay the molecules down in the *a*–*b* plane about the *a* axis by θ_a.
2. Raise EDO-TTF molecules by rotating them about the *b* axis by θ_b.

The first operation erases the second half of the O_{2p} orbital, which is not observed in the STM image. The second one makes the second oxygen of the EDO group observable, which reproduces the widely spread area corresponding to the oxygen pair.

Figure 19B estimated by the rotational model successfully reproduces the overall profile of the STM image. **Figure 21** demonstrates the topographies (A) along the direction connecting the two oxygen atoms of EDO group and (B) along the direction connecting the oxygen and carbon atoms of EDO-TTF molecules stacking along the *b* axis. The simulated profiles of the π charge density successfully reproduce the characteristic profiles of the observed STM image, supporting the above reorientational model. Some dip is found between the two peaks in **Figure 21B**, which is caused by the node of the O_{2p} orbital. This kind of sharp variation would not be reproduced by STM because of the limited resolution of STM caused by the 6*s* orbital of PtIr alloy with the large diameter around 0.3–0.4 nm. Here, θ_b is estimated as ≈ 29° from ≈ 38° in the bulk and 9° observed in the topography of **Figure 21A**. It is, however, difficult to estimate θ_a uniquely from the topography in **Figure 21B**.

http://dx.doi.org/10.5772/63406

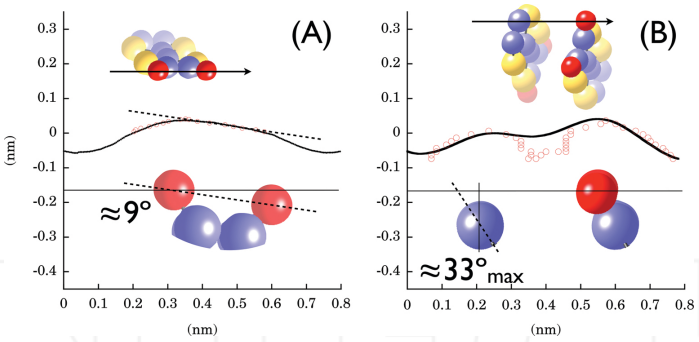

Figure 21. The topographies (A) along the oxygen pair of EDO group and (B) along the oxygen and the carbon atoms of the EDO-TTF molecules. The circles represent the simulated profile at the π charge density of 1×10^{-5} nm^{-3} with θ_a = 18°, θ_b = 29°. The horizontal line indicates the relative position of the oxygen atom.

What these reorientations modify in the π electron system? The θ_b operation cuts the side-by-side 1D network of the sulfur π electrons along the *a* axis. The θ_a one forms one-dimensional π electron band along the stacking *b* axis with the face-to-face pathways of the sulfur pairs in the TTF groups, as shown in **Figure 20**. Furthermore, the 3*p* wavefunction spreads wider along its symmetry axis by <10% than the perpendicular direction, as shown in **Figure 4**. The upper limit of θ_a is estimated as ≈ 18° (≈ 33° from the normal of the *a*–*b* plane) from the shortest distance of ≈ 3.4 Å between the sulfur atoms. Thus, the rotational reconstruction of the EDO-TTF molecules in the surface layer dramatically change the 1D conductive direction from the *a* axis to the *b* axis and can enhance the 1D band width of the π electrons, which stabilizes the surface π electron system and is motivated by the removal of the steric hindrance with the PF_6^- ions of the missing outside double layer.

4. Conclusion

With the wavefunctions of *p* orbitals, we analyzed the STM images of the three charge transfer salts, α-(BEDT-TTF)$_2$I$_3$, β-(BEDT-TTF)$_2$I$_3$, and (EDO-TTF)$_2$PF$_6$ and found three different kinds of reconstructions: (1) charge redistribution, (2) translational reconstruction and (3) rotational reconstruction.

In α-(BEDT-TTF)$_2$I$_3$, the four characteristic protrusions of the STM image are assigned to the end sulfur atoms of the BEDT-TTF molecules in the unit cell and were compared with the simulation based on the 3*p* orbitals of the sulfur atoms. The obtained STM tip heights are analyzed with the scenarios of the structural reconstruction and the charge redistribution. Finally, the charge redistribution similar to the charge ordered state below 135 K in the bulk crystal is found, which is different from the charge disproportionation of the bulk crystal at RT. The origin is ascribed to the gain of the additional cohesive energy in the ground CO state provoked by the missing steric hindrance between the end ethylene groups and the I_3^- ions of

the missing outside double layer, which provides us the insight on the 135 K phase transition of the bulk crystal. This bulk transition from the charge disproportionation to the charge ordered state would be caused by the calming down of the thermal vibration of the end ethylene groups, which assists the BEDT-TTF layers in forming the charge ordered ground state below 135 K.

In β-(BEDT-TTF)$_2$I$_3$, two BEDT-TTF molecules in the unit cell stack with a staggered fashion, in which I_3^- ion is located. Then, the bulk structure suggests the distinctive tip height difference in the unit cell. In contrast, the STM image shows almost the same tip heights in the unit cell, suggesting translational reconstruction up to 0.1 nm to remove the stagger in the unit cell. As a result, the separation between the sulfur atoms of the neighboring BEDT-TTF molecules sizably decreased, which enhances the transfer energy and the cohesive energy of the π electron system. Thus, the missing steric hindrance with I_3^- ions of the missing outside double layer assists the increase of the cohesive energy in the surface BEDT-TTF layer.

In (EDO-TTF)$_2$PF$_6$, the asymmetric molecules of EDO-TTF stack along the *b* axis with head-to-tail type arrangement, but the TTF groups stack with only tiny stagger, in which the π electrons mainly reside. Thus, any sliding reconstruction, as was found in β-(BEDT-TTF)$_2$I$_3$, would not be important even without the steric hindrance with PF_6^- ions. The comparison between the STM image and the simulated topography suggests large rotational reconstruction about both of the *a* axis and the *b* axis. Such a rotational reconstruction drastically changes the direction of the 1D π band from the *a* axis to the *b* axis and largely enhances the π electron band width.

Finally, it is concluded that the surface reconstruction is ascribed to the additional gain of the cohesive energy of the π electron system, provoked by the reduced steric hindrance with the anions of the missing outside double layer. The investigations of the surface states provide not only interesting behaviors of the surface cation layer, but also important insights into the electronic states of a lot of similar charge transfer crystals, as demonstrated in α-(BEDT-TTF)$_2$I$_3$.

Acknowledgements

H. Sakamoto and K. Mizoguchi would like to commemorate Hideyuki Arimoto, who passed away by an obstinate disease in June 2014 and to express our sincere thanks to his contribution to the experiment and analysis of β-(ET)$_2$I$_3$.

Author details

Hirokazu Sakamoto[1*], Eiichi Mori[1,4], Hideyuki Arimoto[1], Keiichiro Namai[1], Hiroyuki Tahara[1], Toshio Naito[2], Taka-aki Hiramatsu[3,5], Hideki Yamochi[3] and Kenji Mizoguchi[1]

*Address all correspondence to: sakamoto@phys.se.tmu.ac.jp

1 Department of Physics, Tokyo Metropolitan University, Hachioji, Tokyo, Japan

2 Department of Chemistry and Biology, Graduate School of Science and Engineering, Ehime University, Matsuyama, Ehime, Japan

3 Research Center for Low Temperature and Materials Sciences, Kyoto University, Sakyo-ku, Kyoto, Japan

4 Present adderss: Functional Material Development Center, Imaging Engine Development Division, Ricoh Co., Ltd, Ebina, Kanagawa, Japan

5 Present adderss: Faculty of Agriculture, Meijo University, Nagoya, Japan

References

[1] E. Mori, H. Usui, H. Sakamoto, K. Mizoguchi, and T. Naito. Charge distribution in the surface BEDT-TTF layer of α-(BEDT-TTF)$_2$I$_3$ at room temperature with scanning tunneling microscopy. *J. Phys. Soc. Jpn.*, 81(1):014707 (1–7), 2011.

[2] A series of the proceedings of International Conference on Science and Technology of Synthetic Metals (ICSM). *Synth. Met.*, Elsevier.

[3] L. B. Coleman, M. J. Cohen, D. J. Sandman, F. G. Yamagishi, A. F. Garito, and A. J. Heeger. Superconducting fluctuations and the Peierls instability in an organic solid. *Solid State. Commun.*, 12(11):1125–1132, 1973.

[4] J. C. Scott, A. F. Garito, and A. J. Heeger. Magnetic susceptibility studies of tetrathiofulvalene-tetracyanoquinodimethan (TTF) (TCNQ) and related organic metals. *Phys. Rev. B*, 10(8):3131–3139, 1974.

[5] D. Jérome, A. Mazaud, M. Ribault, and K. Bechgaard. Superconductivity in a synthetic organic conductor (TMTSF)$_2$PF$_6$. *J. Phys. Lett. (Paris)*, 41(4):95–98, 1980.

[6] T. Ishiguro, K. Yamaji, and G. Saito. *Organic superconductors*. Springer, Berlin; New York, 2nd edition, 1998.

[7] H. Kobayashi, H. Cui, and A. Kobayashi. Organic metals and superconductors based on BETS (BETS = Bis(ethylenedithio)tetraselenafulvalene). *Chem. Rev. (Special issue of Molecular Conductors)*, 104(11):5265–5288, 2004.

[8] M. Yoshimura, H. Shigekawa, H. Yamochi, G. Saito, Y. Saito, and A. Kawazu. Surface structure of the organic conductor β-(BEDT-TTF)$_2$I$_3$ observed by scanning tunneling microscopy. *Phys. Rev. B*, 44(4):1970–1972, 1991.

[9] S. N. Magonov, G. Bar, E. Keller, E. B. Yagubskii, and H.-J. Cantow. Atomic scale surface studies of conductive organic compounds 3. Scanning tunneling microscopy studies of

monocrystals of bis(ethylenedithio)tetrathiafulvalene with triiodide, β-ET_2I_3. *Synth. Met.*, 40:247–256, 1991.

[10] S. N. Magonov, G. Bar, H.-J. Cantow, J. Paradis, J. Ren, M.-H. Whangbo, and E. B. Yagubskii. Scanning tunneling and atomic microscopy images of organic salt conductor $(BEDT\text{-}TTF)_2TlHg(SCN)_4$. *J. Phys. Chem.*, 97:9170–9176, 1993.

[11] S. N. Magonov, G. Bar, H.-J. Cantow, J. Paradis, J. Ren, and M.-H. Whangbo. Characterization of the surfaces of the conducting salts α-$(BEDT\text{-}TTF)_2X$ (X = I_3, IBr_2) by scanning tunneling and atomic force microscopy. *Synth. Met.*, 62:83–89, 1994.

[12] N. Ara-Kato, K. Yase, H. Shigekawa, M. Yoshimura, and A. Kawazu. Scanning tunneling microscopy of TTF-TCNQ single crystal and thin film. *Synth. Met.*, 70(1–3): 1245–1246, 1995.

[13] S. N. Magonov and M.-H. Whangbo. Organic conducting salts. In: *Surface Analysis with STM and AFM*, pp. 189–218. Wiley-VCH Verlag GmbH, Weinheim, 1995.

[14] M. Ishida, K. Hata, T. Mori, and H. Shigekawa. Surface reconstruction formed by ordered missing molecular rows observed on the quasi-one-dimensional organic conductor β-$(BEDT\text{-}TTF)_2PF_6$. *Phys. Rev. B*, 55(11):6773–6777, 1996.

[15] M. Ishida, T. Mori, and H. Shigekawa. Surface charge-density wave on the one-dimensional organic conductor β-$(BEDT\text{-}TTF)_2PF_6$. *Phys. Rev. Lett.*, 83(3):596–599, 1999.

[16] K. Hashimoto, T. Nakayama, N. Yoshimoto, M. Yoshizawa, M. Aono, and I. Yamaguchi. Three distinct terraces on a β-$(ET)_2I_3$ surface studied by scanning tunneling microscopy. *Jpn. J. Appl. Phys.*, 38:L464–L466, 1999.

[17] M. Ishida, O. Takeuchi, T. Mori, and H. Shigekawa. Comparison of the symmetry breaking in the surface molecular structures of one- and two-dimensional bis(ethylenedithio)tetrathiafulvalene compounds. *Jpn. J. Appl. Phys.*, 39(6B-1):3823–2826, 2000.

[18] N. Yoneyama, T. Sasaki, T. Nishizaki, A. M. Troyanovskiy, and N. Kobayashi. Scanning tunneling microscopy study of the anomalous metallic phases in θ-$(BEDT\text{-}TTF)_2$ $MZn(SCN)_4$ (M = Rb, Cs). *J. Low Temp. Phys.*, 142:159–162, 2006.

[19] R. Kondo, S. Kagoshima, N. Tajima, and R. Kato. Crystal and electronic structures of the quasi-two-dimensional organic conductor α-$(BEDT\text{-}TTF)_2I_3$ and its selenium analogue α-$(BEDT\text{-}TSeF)_2I_3$ under hydrostatic pressure at room temperature. *J. Phys. Soc. Jpn.*, 78(11):114714, 2009.

[20] E. B. Yagubskii, I. F. Shchegolev, V. N. Laukhin, P. A. Kononovich, M. V. Kartsovnik, A. V. Zvarykina, and L. I. Buravov. Normal-pressure superconductivity in an organic metal $(BEDT\text{-}TTF)_2I_3$ [bis (ethylene dithiolo) tetrathio fulvalene triiodide]. *JETP Lett.*, 39:12, 1984.

[21] A. Ota, H. Yamochi, and G. Saito. A novel metal-insulator phase transition observed in (EDO-TTF)$_2$PF$_6$. *J. Mater. Chem*., 12(9):2600–2602, 2002.

[22] H. Yamochi and S.-Y. Koshihara. Organic metal (EDO-TTF)$_2$PF$_6$. *Sci. Technol. Adv. Mater*., 10:024305 (1–6), 2009.

[23] T. Kakiuchi, Y. Wakabayashi, H. Sawa, T. Takahashi, and T. Nakamura. Charge ordering in α-(BEDT-TTF)$_2$I$_3$ by synchrotron X-ray diffraction. *J. Phys. Soc. Jpn*., 76(11): 113702, 2007.

[24] T. Mori, A. Kobayashi, Y. Sasaki, H. Kobayashi, G. Saito, and H. Inokuchi. Band structures of two types of (BEDT-TTF)$_2$I$_3$. *Chem. Lett*., 13(6):957–960, 1984.

[25] E. Clementi and D. L. Raimondi. Atomic screening constants from SCF functions. *J. Chem. Phys*., 38(11):2686–2689, 1963.

[26] J. Tersoff and D. R. Hamann. Theory and application for the scanning tunneling microscope. *Phys. Rev. Lett*., 50:1998–2001, 1983.

[27] K. Bender, I. Hennig, D. Schweitzer, K. Dietz, H. Endres, and H. J. Keller. Synthesis, structure and physical properties of a two-dimensional organic metal, di[bis(ethylene-dithiolo)tetrathiofulvalene] triiodide, (BEDT-TTF)$_2$·I$_3$. *Mol. Cryst. Liq. Cryst*., 108(3–4): 359–371, 1984.

[28] P. Guionneau, C. J. Kepert, G. Bravic, D. Chasseau, M. R. Truter, M. Kurmoo, and P. Day. Determining the charge distribution in BEDT-TTF salts. *Synth. Met*., 86:1973–1974, 1997.

[29] K. Murata, M. Tokumoto, H. Anzai, H. Bando, G. Saito, K. Kajimura, and T. Ishiguro. Pressure phase diagram of the organic superconductor β-(BEDT-TTF)$_2$I$_3$. *J. Phys. Soc. Jpn*., 54(6):2084–2087, 1985.

INTECH